Building Conventional Metasurfaces with Unconventional Interband Plasmonics: A Versatile Route for Sustainable Structural Color Generation Based on Bismuth

Fernando Chacon-Sanchez, Carlota Ruiz de Galarreta,* Eva Nieto-Pinero, Marina Garcia-Pardo, Elisa Garcia-Tabares, Nicolas Ramos, Miguel Castillo, Martin Lopez-Garcia, Jan Siegel, Johann Toudert, C. David Wright, and Rosalia Serna*

Plasmonic metasurfaces for structural color generation are typically built using the archetypal noble metals, gold, and silver. These possess plasmonic properties in the visible spectrum due to their inherent high free carrier densities. However, they are much more expensive compared to many other metals and exhibit several nanofabrication issues such as bad surface adhesion or thermally activated inter-diffusion. In this work, it is shown that interband plasmonic materials –whose optical properties are driven by interband transitions instead of free carriers— are appealing candidates for the fabrication of sustainable and cost-efficient metasurfaces for structural coloring. By using bismuth, an environment-friendly interband plasmonic material cheaper than gold and silver, nanodisks gap-plasmon metasurfaces and planar Fabry-Perot cavities are modeled and fabricated, which both successfully enable pure colors that can be robustly tailored upon suitable design. By direct experimental comparison between both types of design in terms of color efficiency, fabrication complexity, and angular robustness; how bismuth-based gap surface plasmon metasurfaces can be excellent candidates for color microprinting is shown, whereas nanolayered Bi Fabry-Pérot cavities are ideal for macroscopic color coatings due to their ease of fabrication and implementation.

1. Introduction

Over the past decades, structural color generation inspired by the natural coloration present in some plants and animals has attracted much attention from the scientific community, as it provides a chemically-stable, and eco-friendly alternative to coloring with classic dyes and pigments.[1] Such artificial structures have been to date proposed for a wide range of applications, including high-resolution color displays,[2–4] anti-counterfeiting,[5] holography,[6] or tunable coloring.[2–4,7,8] Among the wide range of photonic design platforms available to achieve structural coloring, the use of Fabry–Pérot cavities and metasurfaces are arguably two of the most explored options. In this context, Fabry–Pérot cavities and gap-surface plasmon metasurfaces have been substantially employed over the last years, as the resonant behavior of both systems allows for the selective suppression or enhancement of specific spectral bands in the visible spectrum, yielding

F. Chacon-Sanchez, C. R. de Galarreta, E. Nieto-Pinero, M. Garcia-Pardo,
J. Siegel, J. Toudert, R. Serna
Laser Processing Group
Instituto de Óptica
IO-CSIC
Serrano 121, Madrid 28006, Spain
E-mail: cr408@io.cfmac.csic.es; rosalia.serna@csic.es

C. R. de Galarreta, C. D. Wright
Centre for Metamaterial Research and Innovation
University of Exeter
Exeter EX4 4QF, UK

C. R. de Galarreta
Departamento de Física Aplicada
Universidad Autónoma de Madrid
Madrid 28049, Spain

E. Garcia-Tabares
Departamento de Física
Universidad Carlos III de Madrid
Campus Leganés
Madrid 28911, Spain

N. Ramos
Polymat
University of the Basque Country UPV/EHU
Av. de Tolosa 72, Donostia-San Sebastián 20018, Spain

M. Castillo, M. Lopez-Garcia
International Iberian Nanotechnology Laboratory (INL)
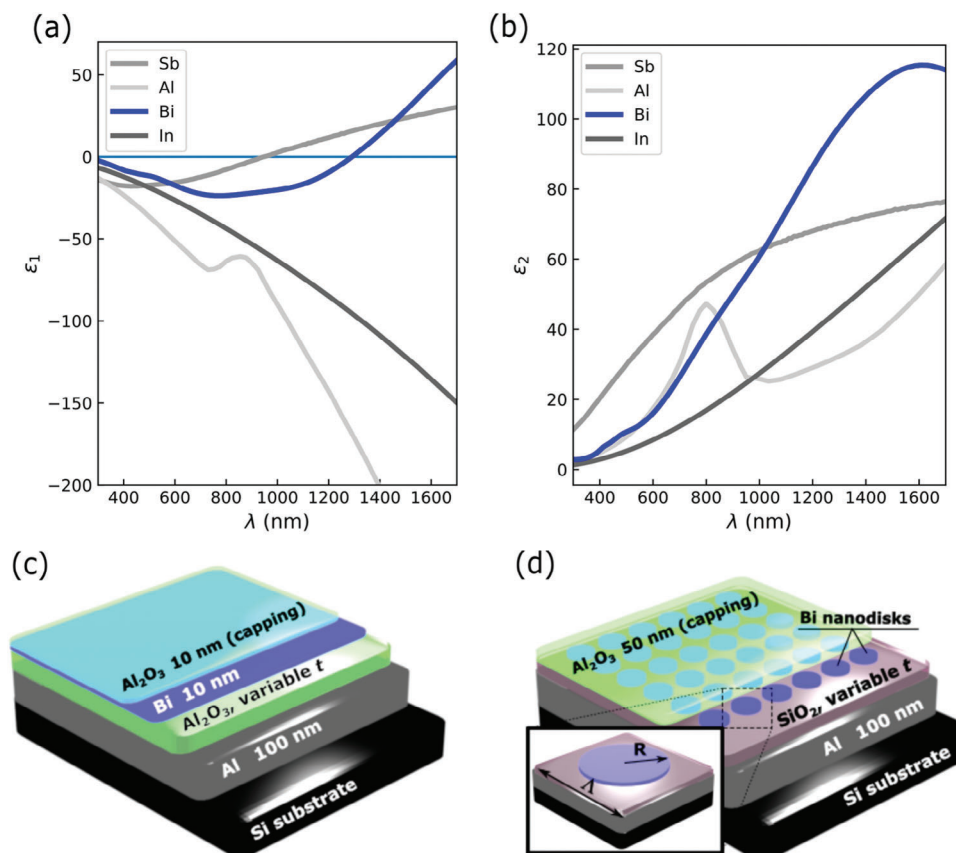Avenida Mestre José Veiga s/n, Braga 4715-330, Portugal

Figure 1. a,b) Real a) and imaginary b) parts of the permittivity for different p-block materials, including Bi,[30] Sb,[51] In, and Al.[52] c,d) Schematics of our Bismuth-based platforms for the realization of colors, namely c) Fabry–Perot cavities, and d) Gap-plasmon metasurfaces.

a particular macroscopic color appearance when illuminated with white light.[4,9–16]

Up to this point, the generation of macroscopic colors using plasmonic structures has predominantly centered on the utilization of noble metals. Here we focus on bismuth, an unconventional plasmonic material that can offer a more environmentally sustainable and economically efficient approach to color production through plasmonic resonances. It is well known that in order to excite plasmonic resonances in the visible spectrum, media with negative real permittivity (ϵ_1) and low-to-moderate imaginary values (ϵ_2) are required, a fact that has traditionally limited the choice of available materials to the evident case of metals with high density of free carriers; such as Au or Ag.[17] Nevertheless, it has been noticed that from an optics point of view, materials with lower free carrier concentrations can not only mimic the plasmonic properties of materials possessing high density of free electrons but also display distinct behaviors in different regions of the electromagnetic spectrum.[17,18] In this context, alternative materials exhibiting inter- and intra-band transitions in the visible or near-infrared spectral regions have been proven to offer a reliable alternative to noble metals for plasmonics-based applications. These include, for instance, non-stoichiometric TiN thin films prepared under specific atmosphere conditions, or materials such as conductive transparent oxides like ITO or AZO, which have been successfully demonstrated as suitable candidates for plasmonics in different parts of the optical electro-

magnetic spectrum.[17,19] However, such materials are composed of multiple elements, thus contrary to noble metals such as Ag or Au, the stoichiometry of as-deposited films needs to be carefully controlled at their deposition stage. Interestingly, as shown in **Figure 1**a,b, single-element p-block materials such as aluminum, indium, antimony, or bismuth can also exhibit suitable plasmonic properties along the ultraviolet (UV), visible(vis), and near infrared (NIR) regimes. In fact, excluding its interband transition located at $\lambda \approx 800$ nm (1.55 eV), aluminum possesses a Drude-like (free electrons) permittivity function, resulting in negative values of ϵ_1 with moderate values of ϵ_2 along the UV–vis spectra. As a result, Al has been already proposed as a cheaper, Complementary metal-oxide semiconductor-compatible plasmonic material alternative to Au and Ag for different applications, including super absorbers,[20] structural coloring,[4,12,21] or beam steering.[22] In line with Al, In exhibits a similar optical behavior (here however without the presence of interband transitions), making it a suitable and competitive candidate for plasmonics in the UV–vis, and even showing superior performance in the UV regime when compared to archetypal plasmonic metals such as Ag. Indeed, recently, the fabrication of ordered, plasmonic nanostructures made of this material has been demonstrated by means of soft imprint lithography combined with electrochemical deposition.[23] However, indium is a relatively rare material, with its abundance in Earth's crust being ≈0.05 ppm only.[24] By looking at alternative, more abundant, p-block materials such

**ADVANCED
SCIENCE NEWS**

www.advancedsciencenews.com

**ADVANCED
OPTICAL
MATERIALS**
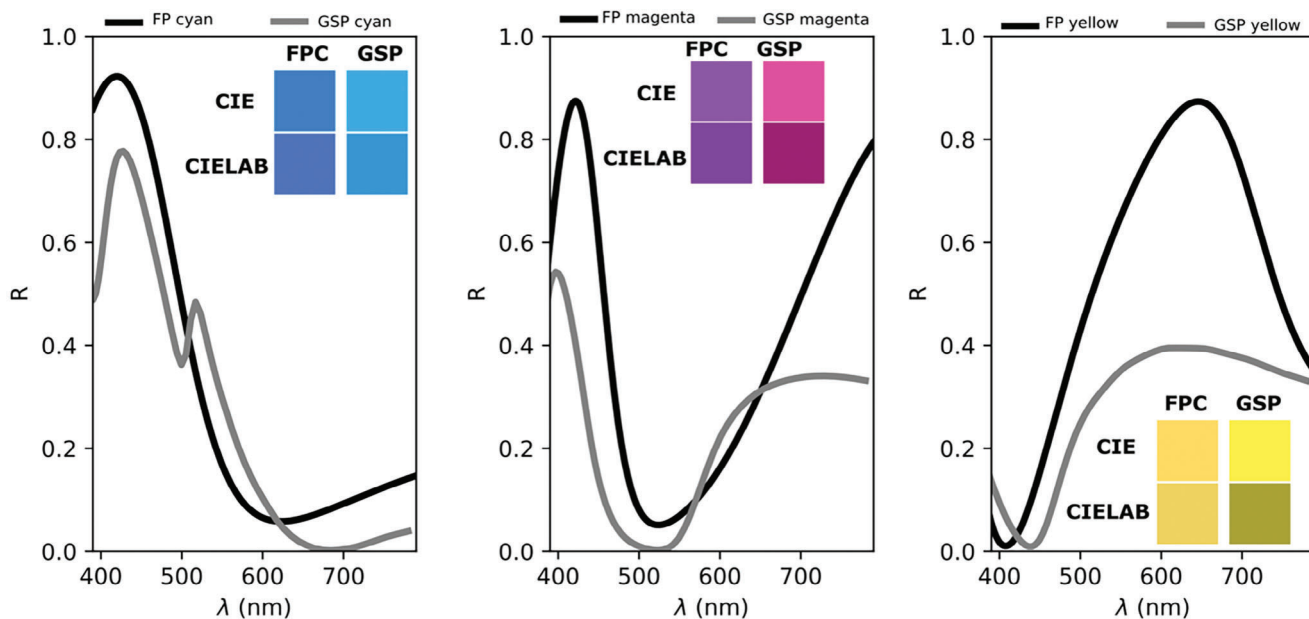
www.advopticalmat.de

Figure 2. Theoretical reflectance of cyan (left) magenta (middle) and yellow (right) for both FP (black curve) and GSP (grey) structures. Insets show the resulting macroscopic colors using both CIE and CIELAB color spaces combined with illuminant D65.

as Sb and Bi, one can realize that they exhibit similar behaviors in the visible spectrum. Indeed, Sb ultra-thin films have been proven as a single-element, solid-state phase-change material,[25] with its amorphous to crystalline phase transition being accompanied by a huge contrast in permittivity functions, yielding applications such as tunable macroscopic coloring and photonic integrated circuits.[26,27] Recently, Bismuth has been also proposed as a suitable candidate for UV-vis plasmonics, while acting as a lossy, high refractive index dielectric in the infrared.[18,28] This originates from the rather unique dielectric function of Bi, as it possesses strong interband transitions in the infrared. As highlighted by the blue curve in Figure 1a,b, Bi exhibits a negative real permittivity in the UV–vis (thus explaining the plasmonic-like behavior of nanostructured Bi),[29,28] while showing a high, positive permittivity in the near-, mid-, and long-wave IR, yielding (real) refractive indices of up to 10.[18,30] Moreover, given its very low toxicity, Bismuth is generally regarded as a sustainable metal and has been proposed as a promising alternative to lead.[31,32] In addition, Bismuth-driven materials are also being currently proposed for applications such as energy storage and conversion, or environmental restoration.[33]

To date, a few Bi-based optical devices have been reported, including plasmonic structural colors with Bi cavities and random nanoparticles in the visible spectrum,[34,35] or perfect absorbers based on metasurfaces,[36] or deeply subwavelength-sized thin Bi films in the IR.[37,38] Moreover, bismuth possesses a relatively low melting point (271 °C), with a significant permittivity contrast between its liquid and solid states, fact that has been recently exploited to study the optical switching and tuning capabilities of Bi embedded nanoparticles experiencing a solid-to-liquid volatile phase-change upon laser irradiation.[39,40] A key issue to exploit the full potential of Bi as a suitable building block for plasmonics is the possibility to fabricate high-quality, ordered nanostructures and thin films. In this context, ultrathin films of Bi prepared by

pulsed laser deposition (PLD) have been proven to exhibit high density and spatial uniformity, with optical properties very close to their bulk state.[29] Such high-quality films can be therefore efficiently used as building blocks for the design of metasurfaces and other nanophotonic devices. Another relevant reason to design Bi-based devices is that, unlike most heavy elements, Bismuth is a sustainable, eco-friendly material,[32,33] and even has potential on devices for environmental restoration, as can be seen in ref. [33].

In this work, we present the design and experimental realization of two different platforms for structural color generation, employing well-controlled thin films and nanostructures of Bi prepared by pulsed laser deposition. The two proposed designs are depicted in Figure 1c,d. The first one (Figure 1c) is a conventional Fabry–Pérot (FP) cavity, consisting of an Al_2O_3 film of thickness t (variable), sandwiched between an optically thick (100 nm) bottom Al mirror, and an upper ultrathin Bi layer (10 nm). The second design is based on the so-called gap surface plasmon (GSP) metasurfaces (**Figure 2d**), which have been successfully employed for local amplitude and phase control over the past decade.[14] The application of this type of structure for plasmonic color generation is quite well-known and extended, either for static[41,42] or dynamic coloring.[43] In analogy to our FP approach, our Bi GSP metasurfaces consist of a thin dielectric (SiO_2) layer of thickness t sandwiched between an Al bottom mirror, and an upper layer of Bi nanodisks arranged in a square lattice of period Λ. For both structures, Bi has been covered with a thin Al_2O_3 layer to prevent oxidation (10 and 40 nm for FP and GSP respectively). While similar devices have been extensively studied using archetypal plasmonic such as Ag, Au, or Al,[4,10,16,9] the use of Bi as the main plasmonic material in such systems remains unexplored. The pros and cons of each type of structure will be discussed in terms of color purity, robustness against the angle of incidence, fabrication complexity, and microprint-

**ADVANCED
SCIENCE NEWS**

www.advancedsciencenews.com

**ADVANCED
OPTICAL
MATERIALS**

www.advopticalmat.de

Table 1. Values of the geometrical variables employed to obtain each structural color for FP and GSP devices.

		Cyan	Magenta	Yellow
Fabry Pérot (FP)	Dielectric layer	$t_{Al2O3} = 108$ nm	$t_{Al2O3} = 220$ nm	$t_{Al2O3} = 165$ nm
	Bi layer	$t_{Bi} = 10$ nm	$t_{Bi} = 10$ nm	$t_{Bi} = 10$ nm
Gap Surface Plasmon (GSP)	Dielectric layer	$t_{SiO2} = 84$ nm	$t_{SiO2} = 29$ nm	$t_{SiO2} = 20$ nm
	Bi structures	$\Lambda = 340$ nm $R = 109$ nm $t_{Bi} = 10$ nm	$\Lambda = 380$ nm $R = 115$ nm $t_{Bi} = 20$ nm	$\Lambda = 380$ nm $R = 101$ nm $t_{Bi} = 20$ nm

ing capabilities. Our results are therefore useful to identify and build the most appropriate design platforms toward structural coloring depending on the application in mind but also highlight the potential of Bi for plasmonics-based nanophotonic devices in the visible spectrum, which could be extrapolated to other above-mentioned unconventional plasmonic materials from the p-block such as antimony or indium in a near future.

2. Results and Discussion

2.1. Bismuth Designs for Structural Color Generation

As briefly described in the introduction, in Figure 1c we showcase our simplest Bi-based design platform, an FP cavity consisting of an optically thick metallic mirror (Al), a dielectric spacer (Al$_2$O$_3$) of variable thickness t, and an ultrathin (10 nm) Bi layer on top. The working principle here is the one of a conventional FP cavity based on optical interference effects. By changing the thickness of the dielectric layer one can tailor absorption at specific spectral bands, provided that the dielectric spacer thickness t satisfies the destructive interference condition at a particular wavelength λ of interest. (i.e., $t_{Al_2O_3} \approx m\lambda/4n_{Al_2O_3}$, with m being an odd integer). On the other hand, as pictured in Figure 1d, the GSP metasurface has a slightly more complex structure. The main difference structure-wise is that the upper lossy plasmonic material (Bi) forms a periodic array of finite-size nanodisks structures (10 nm in thickness). This allows for the excitation of localized surface plasmons which are mirrored on the Al bottom plane, resulting in transverse magnetic dipole moments.[14] This allows for the use of significantly smaller dielectric spacers compared to FP cavities, as revealed by **Table 1**, and discussed previously in the literature.[14,44]

The two Bi-based designer interfaces were optimized following the methodologies described in the section "Design and Analysis of Bi Structures", in order to generate the three subtractive primary colors in reflection (namely cyan, magenta, and yellow). The final geometrical parameters resulting from optimizations for each macroscopic color in our two designer interfaces are listed in Table 1. In Figure 2, we show the resulting reflectance spectra of each color calculated under normal incidence conditions for both the FP (black curve) and the GSP (grey curve) designs. Insets represent their corresponding macroscopic colors employing two different color spaces (CIE and CIELAB, see section "Macroscopic color calculations" for calculations details). As it can be seen, colors obtained from CIE chromaticity diagrams are similar for both designs, exhibiting slightly higher purity for the case of GSP cavities (as shown in Figure S1b, Supporting Information), which can be attributed to their lower minimum reflectivity as well as the higher number of parameters that we can

use to optimize the outcome. However, if we use the CIELAB color space (which takes into account both the chromaticity and the human perception of lightness), GSP colors become darker as a consequence of their lower maximum reflectivity level, while FP colors experience little-to-no change at all. Hence, bismuth-based FPs have a better potential for the generation of high-efficiency colors. As for the case of dyes and pigments, the robustness of the macroscopic color against the angle of incidence is a highly desirable property, especially when the applications in mind imply decorative purposes or displays (i.e., where the macroscopic color needs to be maintained with the viewing angle[1]). Usually, one of the reasons to look for alternatives to FPs is the marked angular dependence of their reflectivity,[15] which inherently occurs due to changes in the optical path difference (thus the cavity phase, and therefore the wavelength at which destructive or constructive interference occurs). In order to investigate the robustness of our devices against the viewing angle, we have also explored the effect of the angle of incidence on the reflectance spectra of our two designs. In **Figure 3**, we compare the reflectance's angular dependence for (unpolarized) white light of both structures for the case of cyan (i.e., where the resulting performance at normal incidence is similar between GSP and FP designs, as previously revealed in Figure 2). For the case of FP designs (Figure 3a), increasing the angle of incidence results in a moderate blueshift, with the reflectance characteristics being well-preserved up to 45°. The angular response of GSP (shown in Figure 3b) reveals slightly smaller robustness of the absolute reflectance against the incidence angle, due to several high Q-factor features arising at off-normal incidence. These originate from Wood–Rayleigh (WR) anomalies excited by the square periodicity of the GSP and occur at the different material interfaces (a more detailed analysis of the WR modes can be found in Section S2, Supporting Information). In Figure 3c we show the reflectance at an incident angle of 30° for both systems, evidencing a drop in reflectance for the case of GSP. Even so, it can be seen that macroscopic colors represented in the inset are nicely maintained at oblique incidence for both systems, making them fairly robust to the viewing angle.

Finally, we also note that despite the periodicity of our GSP being smaller than the wavelength range (thus the structure is non-diffractive at normal incidence), diffraction orders θ_m might couple to the free space at oblique angles of incidence θ_i provided that:

$$\sin\theta_{\pm m} = m\frac{\lambda}{P} \pm \sin\theta_i < |1| \tag{1}$$

In order to investigate possible negative effects of such conditions, diffraction simulations of our structure as a function of the angle of incidence and polarization have been carried out, re-
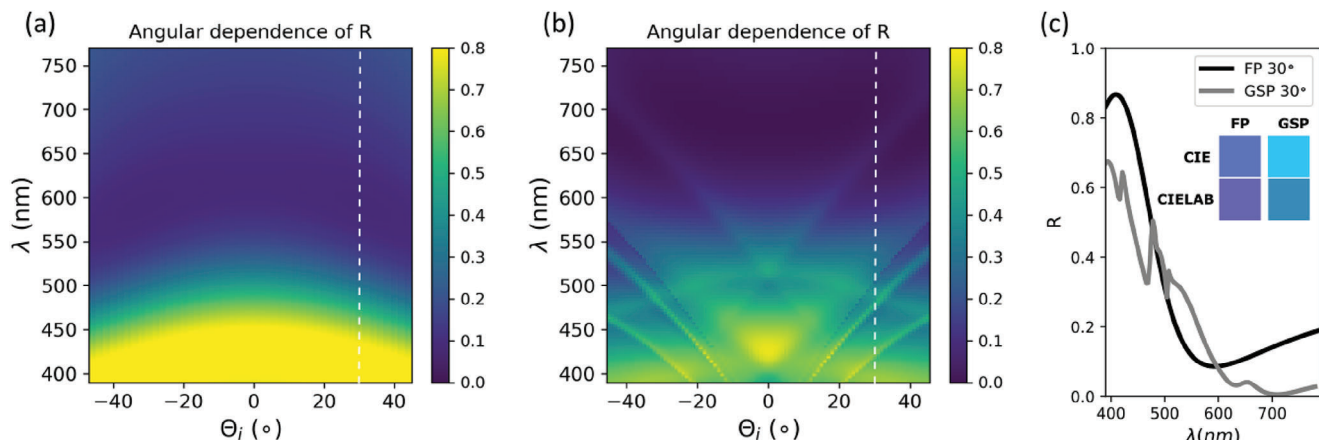
ADVANCED
SCIENCE NEWS

www.advancedsciencenews.com

ADVANCED
OPTICAL
MATERIALS

www.advopticalmat.de

Figure 3. a,b) Angular dependence of the theoretical reflectance spectra (unpolarized), for: a) FP cavities, and b) GSP structures. c) Reflectance at 30° for both FP and GSP structures, and insets showing the corresponding macroscopic colors, revealing a more robust reflectance response of the FP devices, as well as a decrease in brightness (CIELAB colors) for both structures with respect to normal incidence (c.f. Figure 2, left figure).
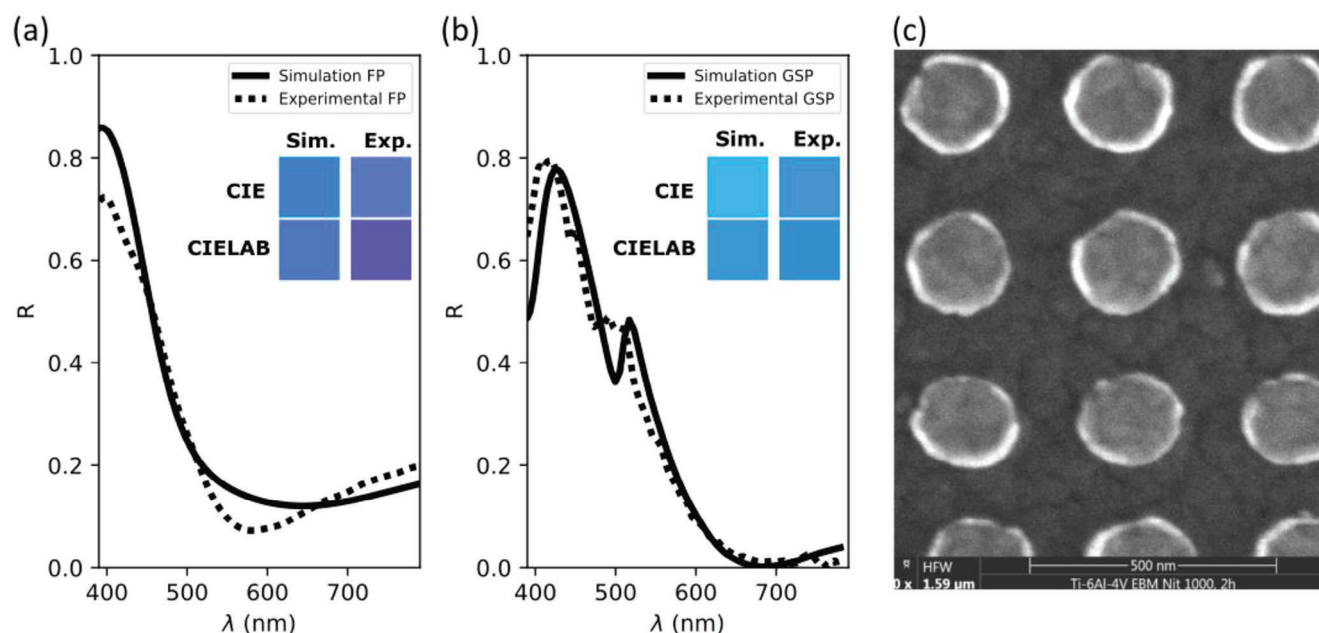

Figure 4. Comparison between experimental and computational reflectance spectra for cyan devices: a) FP at 20° of incidence (unpolarized), and b) GSP at normal incidence. Insets show the corresponding macroscopic colors. c) SEM image of the measured GSP structure.

vealing very low diffraction efficiencies (< 10%) for angles above 8°, occurring at the short part of the visible spectrum only (see Section S3, Supporting Information). Diffraction at oblique incidence by our Bi-based GSP devices is therefore expected to play a negligible role in color perception.

2.2. Experimental Comparison Between the two Bismuth Designer Interfaces

So far, we have numerically compared the optical characteristics of both Bi-based FP and GSP structures, in terms of color purity and angular robustness. In this section, we will proceed to discuss their optical characterization, fabrication complexity (scala-

bility), potential applications, and fidelity between the modeled and experimentally characterized devices (here again for the case of cyan, which is where we find better agreement between optical performances for both approaches).

Figure 4 summarizes the experimental performance of our devices for unpolarized light at near-normal incidence compared to simulations. In particular, Figure 4a shows the calculated (continuous curve) and experimental (dashed curve) reflectance spectra of FP cavities for unpolarized light at 20° (i.e., the minimum angle of incidence available in our spectroscopic ellipsometer, see section "Angle-Dependent Reflectance Measurements: Bismuth FP Cavities"), revealing a very good agreement, with the resulting inset color calculations also exhibiting an excellent matching.
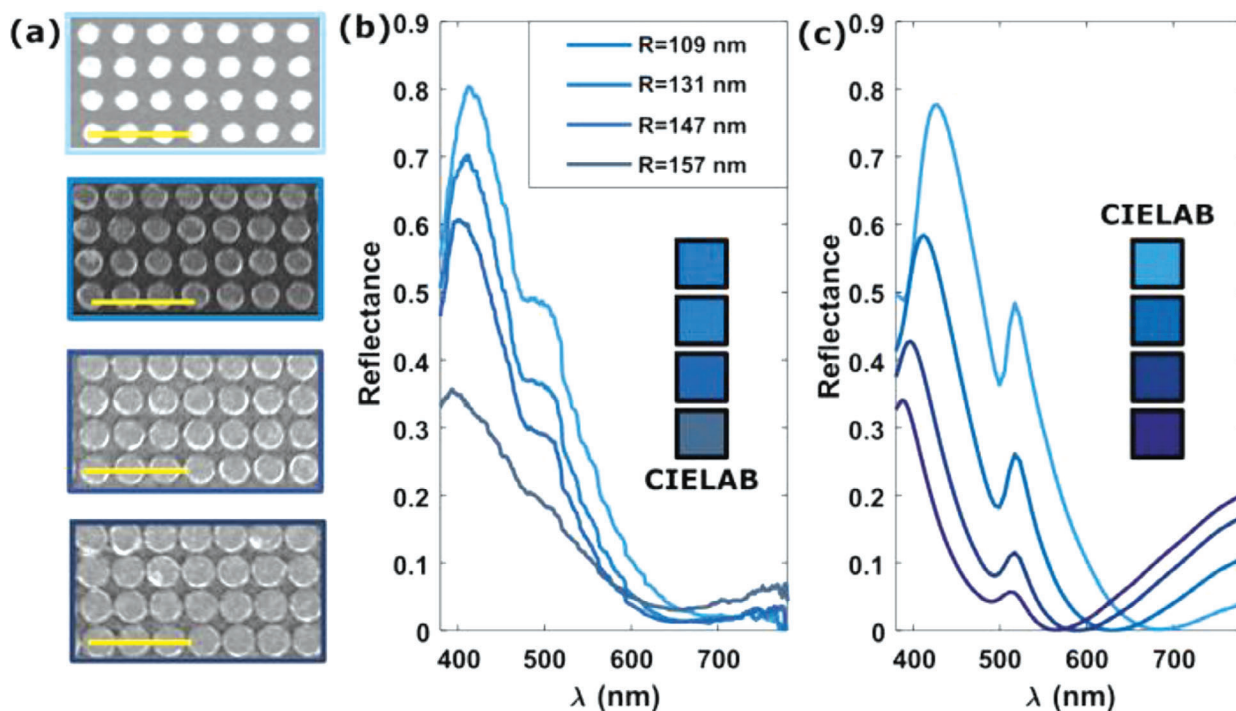
**ADVANCED
SCIENCE NEWS**

www.advancedsciencenews.com

**ADVANCED
OPTICAL
MATERIALS**

www.advopticalmat.de

Figure 5. a) SEM images of 4 different sets of disks having different radii sizes for a fixed period of Λ= 340 nm. The yellow scale bar corresponds to 1 μm. b) Experimental, and c) theoretical reflectance of GSP metasurfaces with different radii shown in (a). Insets show the corresponding macroscopic colors.

For the case of our Bi-based GSP metasurfaces, measurements were performed with a low NA microspectrophotometer at normal incidence, and the results were compared with simulations (represented in Figure 4b). An SEM image of the measured nanodisks is shown in Figure 4c. In line with our FP devices, an excellent correspondence between simulated and measured results is once again evident, and so are the calculated macroscopic colors. However, we note there are some minor divergences between experimental and computational results for both structures, that can be attributed to fabrication issues like disk-to-disk size variations, layer thicknesses (SiO_2, Bi, or Al_2O_3), or roughness (not taken into account in simulations).

In terms of fabrication complexity, as discussed in the Experimental Section, FP structures can be fabricated with a more straightforward process, consisting of depositing the different material layers with pre-designed thicknesses to obtain a desired macroscopic color. As a result, this can be done in a single step for a particular color, however, we also note that the deposition of different colors in a single step requires the use of a moving mask or stencil to spatially control the dielectric thickness. On the other hand, for GSP devices shown in Figure 4c, the fabrication process implies both thin film deposition and patterning via lithography using polymer masks (see section "AFabrication of Bi nanodisks"), which limits its industrial scalability and sustainability, since lithographic structuration over large areas (cm^2) is a long, expensive, and multistep process. However, as opposed to FP, GSP structures allow for color micro-printing in a single deposition step, as the radii of the disks can be spatially tailored during lithography, resulting in changes in the plasmon resonance characteristics (i.e., spectral position and quality factor),[10,14] and

hence the perceived color, as we will see in more detail in the next section.

2.3. Bi-Based GSP Structures: From Color Micro-Printing to Sensing Applications

In order to investigate the color micro-printing capabilities of our Bi-based GSP metasurfaces, a set of devices having different radii of the upper Bi nano-disks (and the same thicknesses and period as our cyan design, as in Table 1) were fabricated. This was carried out in a single lithographic step via spatially varying the size of the printed disks, a procedure that has been already demonstrated for noble metal-based GSP metasurfaces.[44] In **Figure 5b**, we show the resulting measured reflectance spectra at normal incidence, together with their macroscopic colors represented in the inset. As it can be seen, increasing the disk size results in a simultaneous decrease in maximum reflectance, and a slight blueshift of the resonance positions. This turns into strong variations in the perceived color luminosity, also in good agreement with simulations shown in Figure 5c. However, we note that simulated colors shown in the inset tend to also acquire a purple hue as the disk size increases. This difference in hue can be attributed to higher reflectance values obtained in the simulations over the red part of the visible spectrum ($\lambda > 600$ nm) with respect to measured values. As explained in the previous section, we have attributed these differences to experimental factors. In addition to luminosity control, in Section S4 (Supporting Information) of the supplementary material we show how by increasing the thickness of the
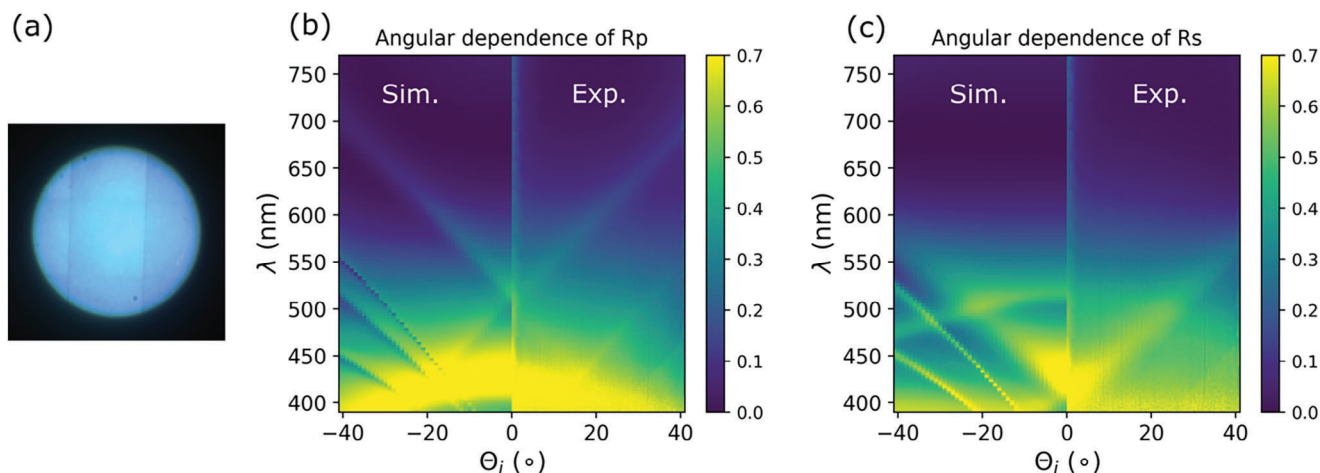
**ADVANCED
SCIENCE NEWS**

www.advancedsciencenews.com

**ADVANCED
OPTICAL
MATERIALS**

www.advopticalmat.de

Figure 6. a) Image of the fabricated GSP under measurement, taken with 40x objective. b,c) Comparison of the angular dependence for the GSP structure between simulations (left) and experimental measurements (right) for p-polarized b) and s-polarized c) light. It can be seen that features on the simulated reflectivity map are preserved for the experimental measurements.

Bi nanodisks, additional color palettes as a function of the disks radii become accessible.

Finally, the reflectance robustness of our Bi GSP metasurfaces against the angle of incidence for both P- and S- polarizations was also experimentally validated by means of back focal plane spectroscopy measurements at the microscale (see section "Angle-Dependent Reflectance Measurements: Bismuth GSP Metasurfaces", for details). **Figure 6**a,b shows bipartite experimental versus simulations reflectance maps for P- and S-polarizations. Once again, a very good agreement between experiments and calculations can be observed, where high Q-factor reflectance features originated from Wood-Rayleigh anomalies (whose dispersion has been previously discussed in Section S2, Supporting Information) are nicely reproduced in experiments. It can be noted that higher Q-factor features are slightly more difficult to distinguish when compared to simulations, which can be explained by the fact that light collection has been always performed by integrating a set of solid angles determined by the NA of the collection lens, whereas simulations were performed assuming plane-wave excitation (i.e., collimated beams). Therefore, for features with high-Q values, higher solid angle resolution is needed, making them more difficult to detect. This experimental limitation is especially patent to this figure but also applies to previous figures (Figures 4,5). Focusing on the optical performance of these structures, the presence of such high-Q features at off-normal incidence is not ideal for angular robustness on the perceived color, but they can find additional suitable applications. For instance, as a result of their inherent sharp, high Q-factor nature, Wood-Rayleigh anomalies are extremely sensitive to environmental changes and indeed have been demonstrated for the detection of small changes in the refractive index (thus concentration) of specific analytes.[45]

2.4. Bi-Based FP Structures: Macroscopic Coloring Gamut

In line with the previous study on tailoring the GSP structure response for applications, we have explored in more detail the use of bismuth-based FP cavities for macroscopic structural coloring. For GSP structures, the fabrication of a whole macroscopic color gamut would prove unnecessarily complicated, whereas the structure and deposition process of FPs discourage color generation as a combination of microscopic CMY pixels. Therefore, the most practical application for Bi-based FP cavities is the possibility of uniform macroscopic structural coloring. In this context, the versatility of Bi FP cavities in terms of achievable color gamut was investigated. Using an ultrathin Bi film as the top cavity layer, we performed variable, graded dielectric deposition to obtain FP cavities that display some of the potential colors (shown in **Figure 7**a). Measuring its reflectance on a grid of just 12 points, we can observe a wide range of achievable colors, measured individually in the right panel of Figure 7a. It is relevant to point out that these are just some of the possible colors, and they can be expanded even more taking into consideration higher Fabry-Pérot interference orders.

Finally, we show the potential benefits of using Bi ultrathin films toward structural coloring, as on Fabry-Perot cavities it doesn't look like the best choice over more conventional plasmonic metals (such as Al, or Ag) with lower losses. However, we find that Bismuth possesses superior performance, specifically for subtractive color generation, when compared with these more extended materials. To elucidate this, In Figure 7b we showcase the reflectance spectrum for two FP cavities with the same structure and using either Al or Bi for the top metallic layer: Al(10 nm) /Al$_2$O$_3$(215 nm)/Al(100 nm) and Bi(10 nm)/Al$_2$O$_3$(215 nm)/Al(100 nm).

At first glance, it can be seen that using an upper ultrathin Al layer results in narrower, high Q-factor destructive interference, which turns into a pale, whitish macroscopic color, as can be observed in the insets in Figure 7b. In contrast, cavities made with ultrathin Bi films exhibit a broader, low Q-factor resonance, resulting in a high-purity yellow color for both CIE and CIELAB color spaces. Such a behavior can be readily explained by carefully examining the optical properties of both materials, represented via their dielectric function in Figure 1a,b. A helpful magnitude to compare these two materials is the plasmonic figure of merit
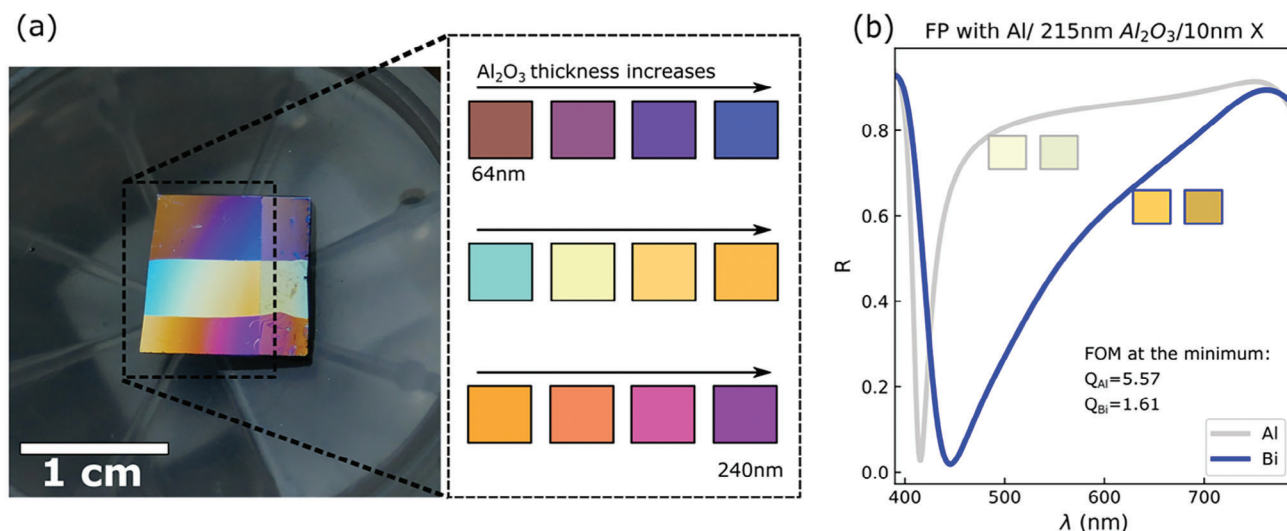
2302130 (7 of 10)

ADVANCED
SCIENCE NEWS

www.advancedsciencenews.com

ADVANCED
OPTICAL
MATERIALS

www.advopticalmat.de

Figure 7. a) The left panel shows an image of the macroscopic view of Bi-based FP cavities with graded Al$_2$O$_3$ deposition, showing a wide variety of achievable colors. On the right panel, we have included the experimentally measured individual macroscopic colors b) Theoretical comparison between FP cavities made with an upper Al layer and an upper Bi layer. Insets show the corresponding macroscopic colors for both systems (CIE-left, CIELAB-right), revealing higher color purities for the case of Bi, as well as the plasmonic figure of merit for each material at the resonance wavelength.

(FOM = -ϵ_1/ϵ_2)[46] of both materials, which is actually the inverse of their dielectric loss tangent ($\delta = \epsilon_2/\epsilon_1$). Values of the FOM for the case of bismuth are indeed several times lower in the visible spectrum when compared to Al (see inset in Figure 7b). This inferior plasmonic/metallic behavior when compared to Al results in an inherent reduction of the quality factor of the resonances when using Bi thin films as the upper metallic mirror on an FP cavity, which translates into the benefit of higher purity subtractive colors.

3. Conclusion

We have introduced and experimentally validated the use of bismuth as a non-expensive and sustainable unconventional plasmonic-like material for structural color generation. To this end, two different designer interfaces – namely Fabry–Pérot cavities and gap surface plasmon metasurfaces — have been explored. Our results reveal that the fabrication of structural colors with both Bi-based FP and GSP devices using thin films deposited via PLD is highly reliable, and has very good fidelity (i.e., good correspondence with theoretical models). Furthermore, the pros and cons of each type of structure have been evaluated in terms of color purity, robustness against the angle of incidence, fabrication complexity, and microprinting capabilities. Regarding the employment of such approaches in real-world applications, the FP approach would be undoubtedly better for uniform macroscopic coloring, due to its fabrication simplicity (thus industrial scalability), and large number of achievable colors. On the other hand, FP cavities lack color microprinting and sensing capabilities, the fact that could be overcome by using the GSP approach, where local color printing can be achieved via spatially varying the size of the Bi disks in a single lithographic step. Moreover, improving angular robustness of Bi-based GSP can be further explored by the use of slightly disordered Bi-nanodisks, preventing

the excitation of Wood-Rayleigh anomalies without compromising the color purity.[47]

We believe our work clarifies the importance of choosing the appropriate design for structural coloring depending on the final application in mind, but also highlights the potential of using unconventional, single-element plasmonic materials toward structural color generation (here in particular for Bi, but alternative plasmonic p-block materials such as In or Sb should be further explored in a near future). Finally, we also highlight that the fabrication of nanostructures via lithography combined with lift-off processes employing PLD has been demonstrated only recently,[48] thus, our work also reinforces the potential of PLD techniques for high-precision lift-off lithographic processes.

4. Experimental Section

Design and Analysis of Bi Structures: The optical properties of thin films such as the ones employed in this work might vary significantly depending on the materials growing conditions (such as the chamber geometry, methodology employed, base and working pressure, deposition rate, etc).[49] Therefore, in order to guarantee the accuracy of both simulations and experiments, the dielectric functions of all as-deposited materials employed in this work (namely Al, SiO$_2$, Al$_2$O$_3$, and Bi) were previously characterized by spectroscopic Ellipsometry (Woolam VASE, spectral range 200–1800 nm). The resulting permittivity functions employed in simulations for all the materials might be found in Section S1 (Supporting Information).

Once the optical properties were properly characterized, the design, optimization, and analysis of Bi devices were carried out employing the commercial finite element methods software package COMSOL Multiphysics for the case of GSP devices, and a transfer matrix method Python code for FP cavities. Fine details about the boundary conditions and optimization processes employed in the GSP model can be also found in Section S1 (Supporting Information).

Macroscopic Color Calculations: Macroscopic color calculations were carried out via Matlab from theoretical and experimental reflectance spectra using both CIE1931 and CIELAB color spaces, and the standard illumi-

nant D65 (Daylight). First, the CIE1931 XYZ coordinates were calculated using standard colorimetry theory as follows:

$$X = \frac{1}{N} \int_{\lambda=380nm}^{\lambda=780nm} I(\lambda) R(\lambda) \bar{x}(\lambda) \, d\lambda \tag{2}$$

$$Y = \frac{1}{N} \int_{\lambda=380nm}^{\lambda=780nm} I(\lambda) R(\lambda) \bar{y}(\lambda) \, d\lambda \tag{3}$$

$$Z = \frac{1}{N} \int_{\lambda=380nm}^{\lambda=780nm} I(\lambda) R(\lambda) \bar{z}(\lambda) \, d\lambda \tag{4}$$

Where $R(\lambda)$ is either the computed or measured reflectance, $I(\lambda)$ is the spectral distribution of the standard illuminant (D65), and $x(\lambda)$, $y(\lambda)$, $z(\lambda)$ are the standard observer tristimulus color matching functions. N is the normalization factor given by:

$$N = \int_{\lambda=380nm}^{\lambda=780nm} I(\lambda) \bar{y}(\lambda) \, d\lambda \tag{5}$$

Finally, the chromaticity coordinates x and y were obtained through the following relations:

$$x = \frac{X}{X+Y+Z}; y = \frac{Y}{X+Y+Z} \tag{6}$$

Fabrication of Bi-Based FP and GSP Devices: Thin Film Deposition: Deposition of Bi and Al_2O_3 was performed by pulsed laser deposition (PLD). An ArF excimer laser ($\lambda = 193$ nm) was used, with a pulse duration of 20 ns, and a repetition rate of 10 and 20 Hz for Bi and Al_2O_3 respectively. The base pressure inside the vacuum chamber was in the range of 1×10^{-7} mbar.

Deposition of Al and SiO_2 was carried out by means of magnetron sputtering. SiO_2 films were prepared by reactive RF sputtering from a pure (99.999%), undoped, silicon target using a commercial sputtering system (Nordiko 2000) in a mixed Ar (50sccm) /O_2 (10 sccm) gas atmosphere. The base pressure was 1.3×10^{-8} mbar, with a working (Ar/O_2) pressure of 8.3×10^{-3} mbar. RF power was set to 200 W, yielding a sputtering rate of 5.9 nm min^{-1}.

For Al films, a custom-built DC sputtering system and pure Al targets (99.999%) were used in a non-reactive Ar atmosphere (20 sccm). The base pressure was 1×10^{-6} mbar, with a working Ar pressure of 1.7×10^{-3} mbar. DC power was set to 170 W, resulting in a deposition rate of 9.9 nm min^{-1}.

Fabrication of Bi Nanodisks: Bi nanodisks were fabricated over 100 μm × 100 μm areas employing standard electron beam lithography and lift-off techniques. First, Si/SiO_2 substrates were cleaned in warm acetone and soft sonication for 10 min, then rinsed in isopropyl alcohol and dried with N_2. Next, the Al/SiO_2 bilayers were prepared via magnetron sputtering (using the processes described previously). The resulting films were spin-coated with a positive photoresist (PMMA diluted in anisole, Microchem 950K A4) at 6000 rpm, yielding a resist thickness of 250 nm which was then baked at 100 °C for 15 min to evaporate the anisole solvent, thus forming a solid PMMA mask. An e-beam lithography process (Nanobeam NB4) combined with lift-off was carried out to transfer the nanodisks patterns onto the resist. Optimum exposing electron doses to obtain the desired pattern dimensions were found to lie between 8 and 9 cm^{-2}. After e-beam lithography, the PMMA regions exposed to electrons were developed in a 15:5:1 solution (isopropryl alcohol: methyl isobutyl ketone: ethyl methyl ketone) for 45 s at room temperature, while gently shaking the sample. Bi nanodisks were then deposited inside the mask by PLD. Finally, the remaining PMMA regions were removed via preliminary PMMA delamination in acetone using a pipette, followed by soft sonication first in warm acetone and then in isopropyl alcohol.

Angle-Dependent Reflectance Measurements: Bismuth FP Cavities: Reflectance of FP cavities as a function of the angle of incidence was measured over small areas (≈0.3mm^2) employing a spectroscopic ellipsometer, and making use of low NA focusing lenses to reduce the cross-section of the (otherwise collimated) incident beam of white light. This allowed

us to measure with more accuracy on thickness gradients discussed in Figure 7a.

Angle-Dependent Reflectance Measurements: Bismuth GSP Metasurfaces: Since GSP metasurfaces were fabricated over areas smaller than the ellipsometer beam, a specialized fourier image spectroscopy setup was employed to obtain angularly resolved reflectance spectra.[50] The setup consisted of a high magnification optical microscope coupled to an external 4f lens system that allowed for the projection of the back focal plane of the objective lens (Nikon Plan Fluor 40×, NA = 0.75 OFN25 DIC M/N2) to the slit of a VIS–NIR spectrograph (Princeton Instruments, Acton SpectraPro SP-2150 and a CCD camera QImaging Retiga R6 USB3.0 Color). All spectra were presented normalized by the reflectance of an optically thick silver mirror.

Supporting Information

Supporting Information is available from the Wiley Online Library or from the author.

Acknowledgements

Conflict of Interest

The authors declare no conflict of interest.

Data Availability Statement

The data that support the findings of this study are available in the supplementary material of this article.

Keywords

[1] Z. Xuan, J. Li, Q. Liu, F. Yi, S. Wang, W. Lu, *The Innovation* **2021**, *2*, 1.
[2] P. Hosseini, C. D. Wright, H. Bhaskaran, *Nature* **2014**, *511*, 206.
[3] C. Ríos, P. Hosseini, R. A. Taylor, H. Bhaskaran, *Adv. Mater.* **2016**, *28*, 4720.
[4] S. G.-C. Carrillo, L. Trimby, Y.-Y. Au, V. K. Nagareddy, G. Rodriguez-Hernandez, P. Hosseini, C. Ríos, H. Bhaskaran, C. D. Wright, *Adv. Opt. Mater.* **2019**, *7*, 1801782.

**ADVANCED
SCIENCE NEWS**

www.advancedsciencenews.com

**ADVANCED
OPTICAL
MATERIALS**

www.advopticalmat.de

[5] N. Dalloz, V. D. Le, M. Hebert, B. Eles, M. A. Flores Figueroa, C. Hubert, H. Ma, N. Sharma, F. Vocanson, S. Ayala, N. Destouches, *Adv. Mater.* **2022**, *34*, 2104054.

[6] R. Zhao, L. Huang, Y. Wang, *PhotoniX* **2020**, *1*, 20.

[7] J.-H. Yoo, H. T. Nguyen, N. J. Ray, M. A. Johnson, W. A. Steele, J. M. Chesser, S. H. Baxamusa, S. Elhadj, J. T. Mckeown, M. J. Matthews, E. Feigenbaum, *ACS Appl. Mater. Interfaces* **2019**, *11*, 22684.

[8] Y.-S. Huang, C.-Y. Lee, M. Rath, V. Ferrari, H. Yu, T. J. Woehl, J. H. Ni, I. Takeuchi, C. Ríos, *Mater. Today Adv.* **2023**, *18*, 100364.

[9] J. C. Blake, S. Rossi, M. P. Jonsson, A. Dahlin, *Adv. Opt. Mater.* **2022**, *10*, 2200471.

[10] R. A. Deshpande, A. S. Roberts, S. I. Bozhevolnyi, *Opt. Mater. Express* **2019**, *9*, 717.

[11] L. Lin, J. Xue, H. Xu, Q. Zhao, W. Zhang, Y. Zheng, L. Wu, Z.-K. Zhou, *Sci. China Mater.* **2021**, *64*, 3007.

[12] D. Franklin, Z. He, P. Mastranzo Ortega, A. Safaei, P. Cencillo-Abad, S.-T. Wu, D. Chanda, *Proc. Natl. Acad. Sci. USA* **2020**, *117*, 13350.

[13] M. Aalizadeh, A. E. Serebryannikov, A. Khavasi, G. A. E. Vandenbosch, E. Ozbay, *Sci Rep* **2018**, *8*, 11316.

[14] F. Ding, Y. Yang, R. A. Deshpande, S. I. Bozhevolnyi, *Nanophotonics* **2018**, *7*, 1129.

[15] M. A. Kats, R. Blanchard, P. Genevet, F. Capasso, *Nat. Mater.* **2013**, *12*, 20.

[16] A. S. Roberts, A. Pors, O. Albrektsen, S. I. Bozhevolnyi, *Nano Lett.* **2014**, *14*, 783.

[17] G. V. Naik, V. M. Shalaev, A. Boltasseva, *Adv. Mater.* **2013**, *25*, 3264.

[18] J. Toudert, R. Serna, *Opt. Mater. Express* **2017**, *7*, 2299.

[19] G. V. Naik, J. Kim, A. Boltasseva, *Opt. Mater. Express* **2011**, *1*, 1090.

[20] S. G.-C. Carrillo, G. R. Nash, H. Hayat, M. J. Cryan, M. Klemm, H. Bhaskaran, C. D. Wright, *Opt. Express* **2016**, *24*, 13563.

[21] J. Olson, A. Manjavacas, L. Liu, W.-S. Chang, B. Foerster, N. S. King, M. W. Knight, P. Nordlander, N. J. Halas, S. Link, *Proc. Natl. Acad. Sci. USA* **2014**, *111*, 14348.

[22] C. R. De Galarreta, A. M. Alexeev, Y.-Y. Au, M. Lopez-Garcia, M. Klemm, M. Cryan, J. Bertolotti, C. D. Wright, *Adv. Funct. Mater.* **2018**, *28*, 1704993.

[23] M. Valenti, M. D. Wobben, Y. Bleiji, A. Cordaro, S. W. Tabernig, M. Aarts, R. D. Buijs, S. R.-K. Rodriguez, A. Polman, E. Alarcón-Lladó, *ACS Appl. Opt. Mater.* **2023**, *1*, 753.

[24] U. Schwarz-Schampera, P. M. Herzig, *Indium*, 1st ed., Springer, Berlin, Heidelberg **2002**.

[25] M. Salinga, B. Kersting, I. Ronneberger, V. P. Jonnalagadda, X. T. Vu, M. Le Gallo, I. Giannopoulos, O. Cojocaru-Mirédin, R. Mazzarello, A. Sebastian, *Nat. Mater.* **2018**, *17*, 681.

[26] Z. Cheng, T. Milne, P. Salter, J. S. Kim, S. Humphrey, M. Booth, H. Bhaskaran, *Sci. Adv.* **2021**, *7*, eabd7097.

[27] S. Aggarwal, T. Milne, N. Farmakidis, J. Feldmann, X. Li, Y. Shu, Z. Cheng, M. Salinga, W. H. Pernice, H. Bhaskaran, *Nano Lett.* **2022**, *22*, 3532.

[28] J. Toudert, R. Serna, M. Jiménez De Castro, *J. Phys. Chem. C* **2012**, *116*, 20530.

[29] J. Toudert, R. Serna, C. Deeb, E. Rebollar, *Opt. Mater. Express* **2019**, *9*, 2924.

[30] J. Toudert, R. Serna, I. Camps, J. Wojcik, P. Mascher, E. Rebollar, T. A. Ezquerra, *J. Phys. Chem. C* **2017**, *121*, 3511.

[31] R. Wang, H. Li, H. Sun, in *Encyclopedia of Environmental Health*, (Ed: J. Nriagu), Elsevier, Amsterdam **2019**, pp. 415–423.

[32] R. Mohan, *Nat. Chem.* **2010**, *2*, 336.

[33] S. Adhikari, S. Mandal, D.-H. Kim, *Small* **2023**, *19*, 2206003.

[34] A. Ghobadi, H. Hajian, M. Gokbayrak, B. Butun, E. Ozbay, *Nanophotonics* **2019**, *8*, 823.

[35] Y.-P. Chen, C.-C. Lai, W.-S. Tsai, *Opt. Express* **2020**, *28*, 24511.

[36] I. Ozbay, A. Ghobadi, B. Butun, G. Turhan-Sayan, *Opt. Lett.* **2020**, *45*, 686.

[37] J. Toudert, R. Serna, M. G. Pardo, N. Ramos, R. J. Peláez, B. Maté, *Opt. Express* **2018**, *26*, 34043.

[38] A. Ghobadi, B. Butun, I. Ozbay, G. Turhan-Sayan, *Opt. Lett.* **2020**, *45*, 686.

[39] M. Alvarez-Alegria, J. Siegel, M. Garcia-Pardo, F. Cabello, J. Toudert, E. Haro-Poniatowski, R. Serna, *Adv. Opt. Mater.* **2022**, *10*, 2101405.

[40] M. Garcia-Pardo, E. Nieto-Pinero, A. K. Petford-Long, R. Serna, J. Toudert, *Nanophotonics* **2020**, *9*, 885.

[41] K. Kumar, H. Duan, R. S. Hegde, S. C. W. Koh, J. N. Wei, J. K. W. Yang, *Nat. Nanotechnol.* **2012**, *7*, 557.

[42] K. Xiong, G. Emilsson, A. Maziz, X. Yang, L. Shao, E. W. H. Jager, A. B. Dahlin, *Adv. Mater.* **2016**, *28*, 9956.

[43] F.-Z. Shu, F.-F. Yu, R.-W. Peng, Y.-Y. Zhu, B. Xiong, R.-H. Fan, Z.-H. Wang, Y. Liu, M. Wang, *Adv. Opt. Mater.* **2018**, *6*, 1700939.

[44] A. S. Roberts, R. A. Deshpande, S. I. Bozhevolnyi, *Opt. Mater. Express* **2019**, *9*, 717.

[45] M. Eitan, Z. Iluz, Y. Yifat, A. Boag, Y. Hanein, J. Scheuer, *ACS Photonics* **2015**, *2*, 615.

[46] Y. Gutiérrez, A. S. Brown, F. Moreno, M. Losurdo, *J. Appl. Phys.* **2020**, *128*, 080901.

[47] P. Cencillo-Abad, D. Franklin, P. Mastranzo-Ortega, J. Sanchez-Mondragon, D. Chanda, *Sci. Adv.* **2023**, *9*, eadf7207.

[48] A. Gassenq, Y. Guyot, E. Cleyet-Merle, S. Cueff, H.-S. Nguyen, A. Pereira, *Appl. Phys. A* **2023**, *129*, 268.

[49] E. Gemo, S. V. Kesava, C. Ruiz De Galarreta, L. Trimby, S. García-Cuevas Carrillo, M. Riede, A. Baldycheva, A. Alexeev, C. D. Wright, *Opt. Mater. Express* **2020**, *10*, 1675.

[50] W. P. Wardley, J. W. Goessling, M. Lopez-Garcia, *Biomimetics* **2022**, *7*, 107.

[51] Z. Cheng, T. Milne, P. Salter, J. S. Kim, S. Humphrey, M. Booth, H. Bhaskaran, *Sci Adv* **2021**, *7*, eabd7097.

[52] *Handbook of Optical Constants of Solids* (Ed: E. D. Palik), Academic Press, Cambridge **2012**.